ACS OMEGA

http://pubs.acs.org/journal/acsodf

Article

Novel Type-II Heterojunction Binary Composite (CdS/AgI) with Outstanding Visible Light-Driven Photocatalytic Performances toward Methyl Orange and Tetracycline Hydrochloride

Iftekhar Ahmad, Mohammad Muneer,* Abdelrahman S. Khder, and Saleh A. Ahmed*

Cite This: *ACS Omega* 2023, 8, 22708−22720

Read Online

ACCESS | Metrics & More | Article Recommendations | Supporting Information

ABSTRACT: In this study, an effective type-II heterojunction CdS/AgI binary composite was constructed by an *in situ* precipitation approach. To validate the successful formation of heterojunction between AgI and CdS photocatalysts, the synthesized binary composites were characterized by various analytical techniques. UV−vis diffuse-reflectance spectroscopy (UV−vis DRS) revealed that heterojunction formation led to a red shift in the absorbance spectra of the CdS/AgI binary composite. The optimized 20AgI/CdS binary composite showed a least intense photoluminescence (PL) peak indicating highly improved charge carrier (e^-/h^+ pairs) separation efficiency. The photocatalytic efficiency of the synthesized materials was assessed based on the degradation of methyl orange (MO) and tetracycline hydrochloride (TCH) in the presence of visible light. Compared to bare photocatalysts and other binary composites, the 20AgI/CdS binary composite showed the highest photocatalytic degradation performances. Additionally, the trapping studies showed that superoxide radical anion ($O_2^{\bullet-}$) was the most dominant active species involved in photodegradation processes. Based on the results of active species trapping studies, a mechanism was proposed to describe the formation of type-II heterojunctions for CdS/AgI binary composite. Overall, the synthesized binary composite has tremendous promise for environmental remediation due to its straightforward synthesis approach and excellent photocatalytic efficacy.

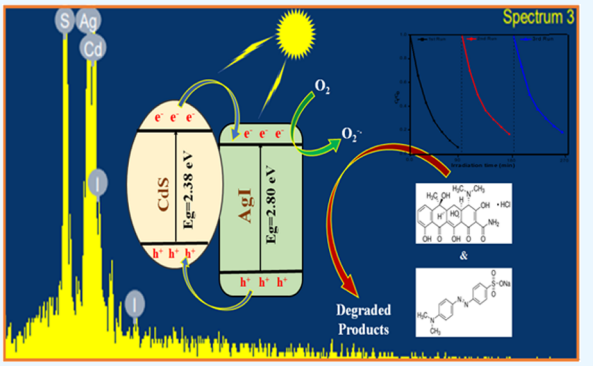

1. INTRODUCTION

Owing to its advantages in the degradation of wastewater contaminants, the semiconductor-based photocatalysis approach that utilizes visible light has recently gained a lot of interest.[1−4] The construction of potent photocatalysts with exceptional stability and reusability is therefore crucial for the photodegradation processes. Several studies have shown that photocatalytic activity depends on the absorption of light and the separation of charge carriers.[5] However, charge carrier separation in a semiconductor is extremely difficult in its unmodified state. TiO_2, for instance, has drawn a lot of interest because of its ability to tackle environmental issues.[6,7] Unfortunately, the large energy bandgap of TiO_2 (3.2 eV) restricts its optical absorption in the ultraviolet portion of the solar spectrum, which is only about 4% of the total solar energy.[8−10] Visible light regions of the solar spectrum accounted for almost 43%, and therefore making visible light active photocatalysts with small bandgap could be very effective for photodegradation processes.[11] However, synthesizing visible light active semiconductor materials is not sufficient as the recombination rate of charge carriers is very high due to the small band gap energy.[12] This problem was addressed using various strategies, such as doping metals and nonmetals,[13,14] co-depositing metals on semiconductor surfaces,[15−17] and coupling of two or more semiconductors to create binary[18,19] and ternary[20,21] heterojunctions. A key strategy in photocatalytic processes for pollutant degradation is the construction of type-II heterostructure composite photocatalysts by coupling appropriate semiconductors.[22,23]

One of the most active photocatalysts with the broader visible light response is thought to be the significant semiconductor metal chalcogenide known as CdS.[24] The active sites of CdS in photocatalytic reactions include surface defects, facet edges and corners, and interfacial sites with other photocatalysts.[25] The unsatisfactory photocatalytic performances of pristine CdS is caused by the fast recombination of photoinduced charge carriers.[26] Additionally, the photocorrosion of CdS during irradiation processes reduced its usefulness as a photocatalyst. To overcome these drawbacks, intensive research has been conducted to improve the photocatalytic capability of CdS. Constructing heterostructures

Received: March 6, 2023
Accepted: May 31, 2023
Published: June 9, 2023

through coupling with other semiconductors is one of the major techniques for addressing the recombination of charge carriers and photocorrosion in CdS.[27] The heterojunction formation between the photocatalysts with suitable band edge potentials significantly improves the performances for photocatalytic degradation. Shao et al. showed that g-C_3N_4/CdS nanocomposite possessed superior photocatalytic activity toward cloxacillin antibiotic degradation compared to pristine g-C_3N_4 and CdS.[28] El-Katori et al. synthesized CdS/SnO_2 binary composites, which demonstrated good photocatalytic capabilities for the degradation of methylene blue.[29] Tong et al. showed that p-nitrophenol degraded using Si−α-Fe_2O_3/CdS composite more efficiently than α-Fe_2O_3 and CdS.[30] In the current study, the *in situ* precipitation method was used to synthesize a binary composite CdS/AgI for photodegradation applications. AgI photocatalyst was chosen to couple with CdS to establish a type-II heterojunction because the band locations of both semiconductors were compatible. To the best of our knowledge, no scientific literature has yet reported the synthesis of CdS/AgI binary composite. The synthesized photocatalysts were characterized using different analytical techniques to determine the chemical compositions and structural features. The CdS/AgI binary composite is an innovative and promising photocatalyst for the degradation of organic pollutants such as methyl orange and tetracycline hydrochloride. Its unique properties and synergistic effects make it a potential candidate for environmental remediation applications. The binary composite can be easily separated from the reaction mixture and reused multiple times, leading to a reduction in the cost and environmental impact. The photocatalytic mechanism of the CdS/AgI binary composite was also explained, and it was based on the findings of quenching studies, band edge potential calculations, and valence band XPS observations.

2. RESULTS AND DISCUSSION

2.1. XRD Analysis. The X-ray diffraction (XRD) technique was used to assess the purity of the prepared samples as well as their crystallographic structures. The XRD patterns of CdS, AgI, 10AgI/CdS, 20AgI/CdS, and 30AgI/CdS are shown in Figure 1. The XRD pattern of CdS shows distinct hexagonal wurtzite diffraction peaks located at 2θ = 24.9° (100), 26.5° (002), 28.2° (101), 36.64° (102), 43.8° (110), 47.9° (103), 51.9° (112), and 52.91° (201) (JCPDS 41-1049).[31,32] The diffraction peaks at 2θ = 22.31, 23.68, 25.35, 32.80, 39.28, 42.59, and 46.38° resembled well the (100), (002), (101), (102) (110), (103), and (112) planes of AgI, respectively (JCPDS 09-0374).[33,34] The composites also showed distinct XRD peaks for CdS and AgI, which may indicate that AgI was well dispersed in the synthesized materials. The inherent structures of the raw materials are therefore thought to be unaffected by the precipitation procedure. Additionally, the diffraction peaks of AgI and CdS in the composite materials are in the same place and closely match those of the standard card, indicating that the crystal phase was unaltered during the AgI/CdS synthesis. An increase of AgI content from 10 to 30% was also observed as the peaks related to the AgI were more prominent in the case of 30AgI/CdS.

2.2. Fourier Transform Infrared Spectroscopy. FT-IR spectroscopy was employed to investigate the functional groups and distinct chemical bonding in the synthesized materials. Figure 2 shows the FT-IR spectra of the as-prepared pure AgI, CdS, and 20AgI/CdS binary composite. FTIR

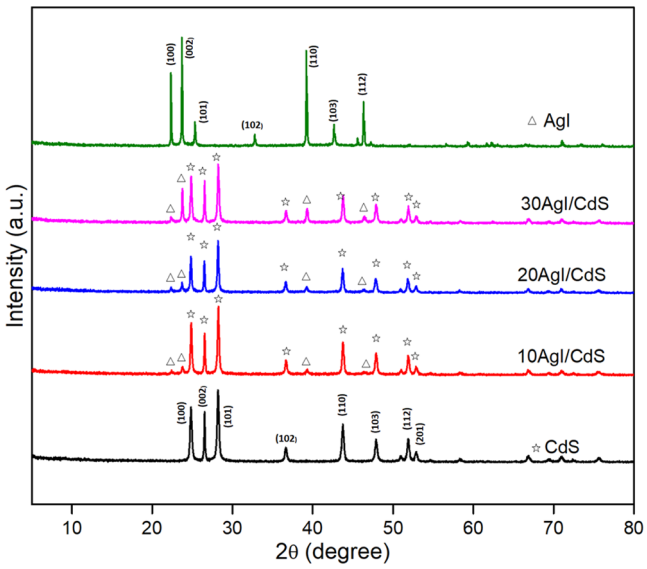

Figure 1. XRD patterns of pure CdS, AgI, and 10AgI/CdS, 20AgI/CdS, and 30AgI/CdS binary nanocomposites.

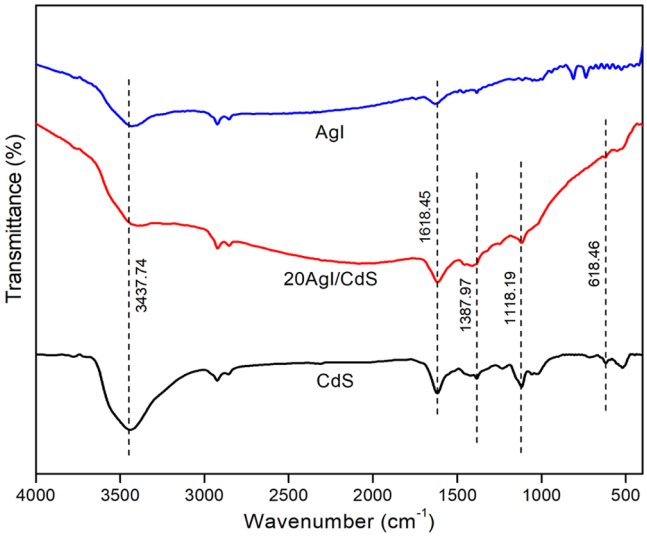

Figure 2. FTIR spectra of pure CdS, AgI, and 20AgI/CdS binary composite.

spectra of CdS and 20AgI/CdS binary composite showed distinct peaks for adsorbed water because of the stretching (3437.74 cm^{-1}) and bending (1618.45 cm^{-1}) vibration modes.[35] The bands at 1387.97, 1118.19, and 618.46 cm^{-1} correspond to the anticipated IR absorption of the Cd−S bond, confirming the formation of CdS.[36,37] A strong band at 3429 cm^{-1} and a relatively weaker band at 1634 cm^{-1} in the FTIR spectra of AgI were identified to be the stretching and bending modes of vibration of the hydroxyl groups of water molecules adsorbed at the surface of the nanoparticles.[38] The distinctive bands of AgI emerged between 400 and 600 cm^{-1}.[39] Due to the low content, AgI bands were not visible in the 20AgI/CdS binary composite, but further analysis using XPS and EDS mapping proved the presence of AgI in the composite material.

2.3. Optical Properties. The optical features of the composite materials were examined by UV−vis DRS spectral analysis, as shown in Figure 3a. Pure AgI showed significant

https://doi.org/10.1021/acsomega.3c01517
ACS Omega 2023, 8, 22708−22720

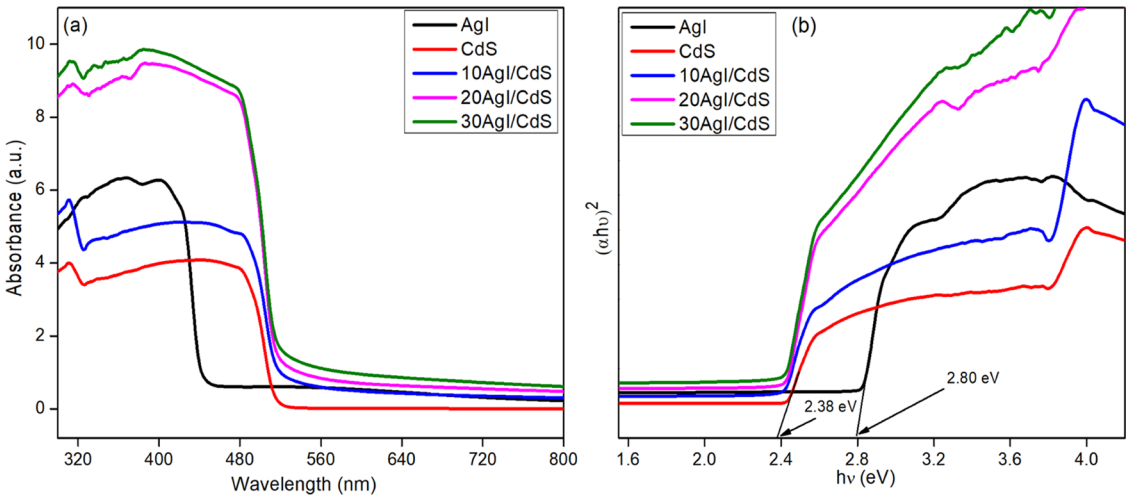

Figure 3. (a) UV−vis DRS spectra of pure AgI, CdS, and 10AgI/CdS, 20AgI/CdS, and 30AgI/CdS binary composites and (b) their corresponding Tauc's plot.

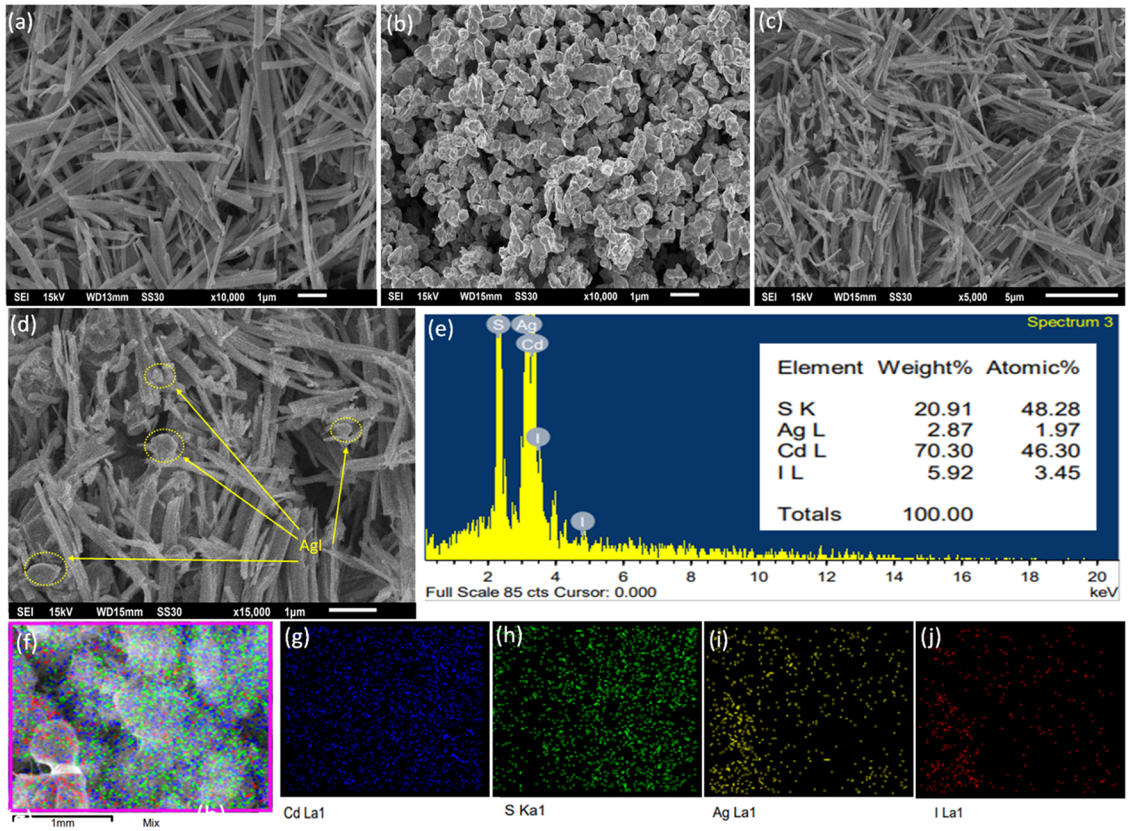

Figure 4. SEM images of pure CdS (a), AgI (b), and 20AgI/CdS binary composite (c, d). EDX spectra of 20AgI/CdS (e) and elemental mapping of 20AgI/CdS (f–j).

absorption in the visible region at a wavelength of about 460 nm, consistent with the earlier result.[40] The remarkable visible light nature of pure CdS is demonstrated by its absorption edge at around 521 nm.[41] The incorporation of AgI shifted the absorption spectra of the binary composites toward the longer-wavelength region. As a result, the binary composites may respond to visible light more readily, demonstrating an important interaction between AgI and CdS catalysts.

The bandgap energies of AgI, CdS, and 10AgI/CdS, 20AgI/CdS, and 30AgI/CdS binary composites were achieved by the following formula (formula 1)[42,43]

$$ahv = A\ (hv - E_g)^{n/2} \quad (1)$$

where A, h, υ, E_g, and a are constant, Planck constant, light frequency, bandgap, and absorption coefficient, respectively. Since $n = 1$ for a direct transition and $n = 4$ for an indirect transition, the value of n determines the electronic transitions in semiconductors.[44,45] The reported n values for both pure AgI and CdS were found to be 1.[46,47] The bandgap of pure AgI and CdS was calculated to be 2.80 and 2.38 eV, respectively, as shown in Figure 3b. These results coincide with the findings that were reported in the earlier literature.[48−50] Furthermore,

https://doi.org/10.1021/acsomega.3c01517
ACS Omega 2023, 8, 22708−22720

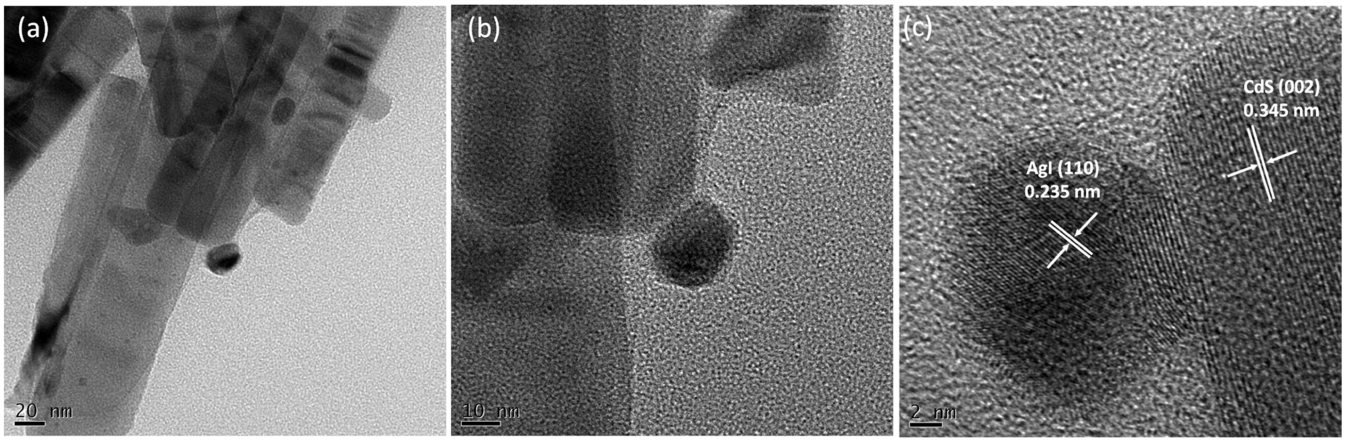

Figure 5. TEM (a, b) and HRTEM (c) images of the 20AgI/CdS binary composite.

the band gap energy for 20AgI/CdS was determined to be 2.35 eV, demonstrating the enhanced visible light absorption capability of the binary composites.

2.4. SEM, EDX, and TEM Analyses. Scanning electron microscopy (SEM) was used to examine the surface characteristics of all the pure photocatalysts and the binary composite, and the findings are displayed in Figure 4. SEM images of the pure AgI, CdS, and optimized 20AgI/CdS binary composite at high and low magnifications are shown in Figure 4a−d. The morphology of the CdS has a nanorod-like structure (Figure 4a), whereas AgI appears to be an irregular spherical type (Figure 4b). The morphology of composite materials revealed in Figure 4c,d demonstrates that AgI nanoparticles are located on the surfaces of CdS nanorods. The EDX spectra and weight percentages of the elements found in the 20AgI/CdS binary composite are shown in Figure 4e. The Ag, I, Cd, and S elements are uniformly distributed in the 20AgI/CdS binary composite, as proved by EDX elemental mapping (Figure 4f−j). The transmission electron micrographs (TEM), as well as the high-resolution TEM (HRTEM) of the binary composite are presented in Figure 5. The TEM images show that the two materials are in close contact, and a noticeable heterojunction was established between AgI and CdS (Figure 5a,b). The AgI nanoparticles are located in close proximity to the CdS nanorod, which may facilitate electron and hole transfer between the two materials. Measurements of the lattice fringes of an HRTEM (Figure 5c) revealed interlayer distances of 0.345 nm for CdS (002) planes and 0.235 nm for AgI (110) planes.

2.5. X-ray Photoelectron Spectroscopy. XPS technique was used to evaluate the chemical states and elemental compositions of the AgI, CdS, and optimized 20AgI/CdS binary composite, as shown in Figure 6. The survey scan spectrum clearly shows the existence of Ag, I, Cd, and S in the 20AgI/CdS binary composite (Figure 6a). The C 1s peak observed in AgI, CdS, and 20AgI/CdS spectra are the result of adventitious carbon.[51] High-resolution XPS spectra were also used to demonstrate the elements and their chemical states for the 20AgI/CdS binary composite, and the findings are shown in Figure 6b−e. The high-resolution XPS spectrum of Ag 3d revealed two peaks, Ag $3d_{5/2}$ and Ag $3d_{3/2}$, with binding energies of 368.03 and 374.03 eV, respectively (Figure 6b).[52] The binding energies for I $3d_{5/2}$ and I $3d_{3/2}$ in AgI were found at 619.46 and 630.96 eV, respectively (Figure 6c).[53] The spectrum for Cd 3d under high-resolution display two peaks at 405.32 and 412.18 eV, corresponding to the Cd $3d_{5/2}$ and Cd $3d_{3/2}$ states, respectively (Figure 6d).[54] The XPS spectrum of S 2p exhibited two peaks at 162.69 and 161.53 eV, representing S $2p_{1/2}$ and S $2p_{3/2}$ electronic states, respectively (Figure 6e).[55] A comparison of the binding energies of the elements found in pure and 20AgI/CdS binary composite is presented in Figure S1. A small shift toward the higher binding energy was observed in the case of 20AgI/CdS, showing strong interactions between the AgI and CdS photocatalysts.

2.6. PL Spectral and EIS Analysis. The separation efficiency and charge transfer resistance of the synthesized photocatalysts were measured using PL spectral analysis and electrochemical impedance spectroscopy (EIS), and the results are shown in Figure 7a,b. The recombination rate of photogenerated electron−hole pair profoundly impacts the efficiency of semiconductor materials as photocatalysts.[56,57] It is particularly known that a rapid rate of photogenerated charge carriers recombination results in a strong photoluminescence signal.[58] Figure 7a shows the photoluminescence signal for pure and binary composites at an excitation wavelength of 330 nm. Pure CdS and AgI showed strong PL signals due to the rapid recombination of photo-excited e^-/h^+ pairs. Low PL intensities in binary composites (10AgI/CdS, 20AgI/CdS, and 30AgI/CdS) demonstrated that composite materials are significantly more efficient at separating photo-excited e^-/h^+ pairs.

The charge-transfer resistance capacity of the synthesized materials was examined using EIS. Figure 7b displays the EIS Nyquist plots for CdS, AgI, and 20AgI/CdS. It is well known from the literature that materials with smaller semicircle diameters in EIS Nyquist plots exhibit the lowest charge-transfer resistance and, as a result, show better e^-/h^+ pair separation.[59−61] The smallest semicircle diameter of the 20AgI/CdS binary composite indicated the successful separation of photogenerated e^-/h^+ pairs via interfacial charge transfer.

2.7. Photocatalytic Performances. The photocatalytic efficiency of the CdS/AgI binary composites under simulated visible light irradiation was evaluated by attempting the degradation of MO and TCH pollutants. The results of the photocatalytic degradation experiments are shown in Figure 8. Prior to the photocatalytic degradation experiment, an adsorption−desorption equilibrium was achieved by sonicating the target pollutant with suspended photocatalyst for 15 min, followed by 25 min of stirring in the dark at room temperature.

https://doi.org/10.1021/acsomega.3c01517
ACS Omega 2023, 8, 22708−22720

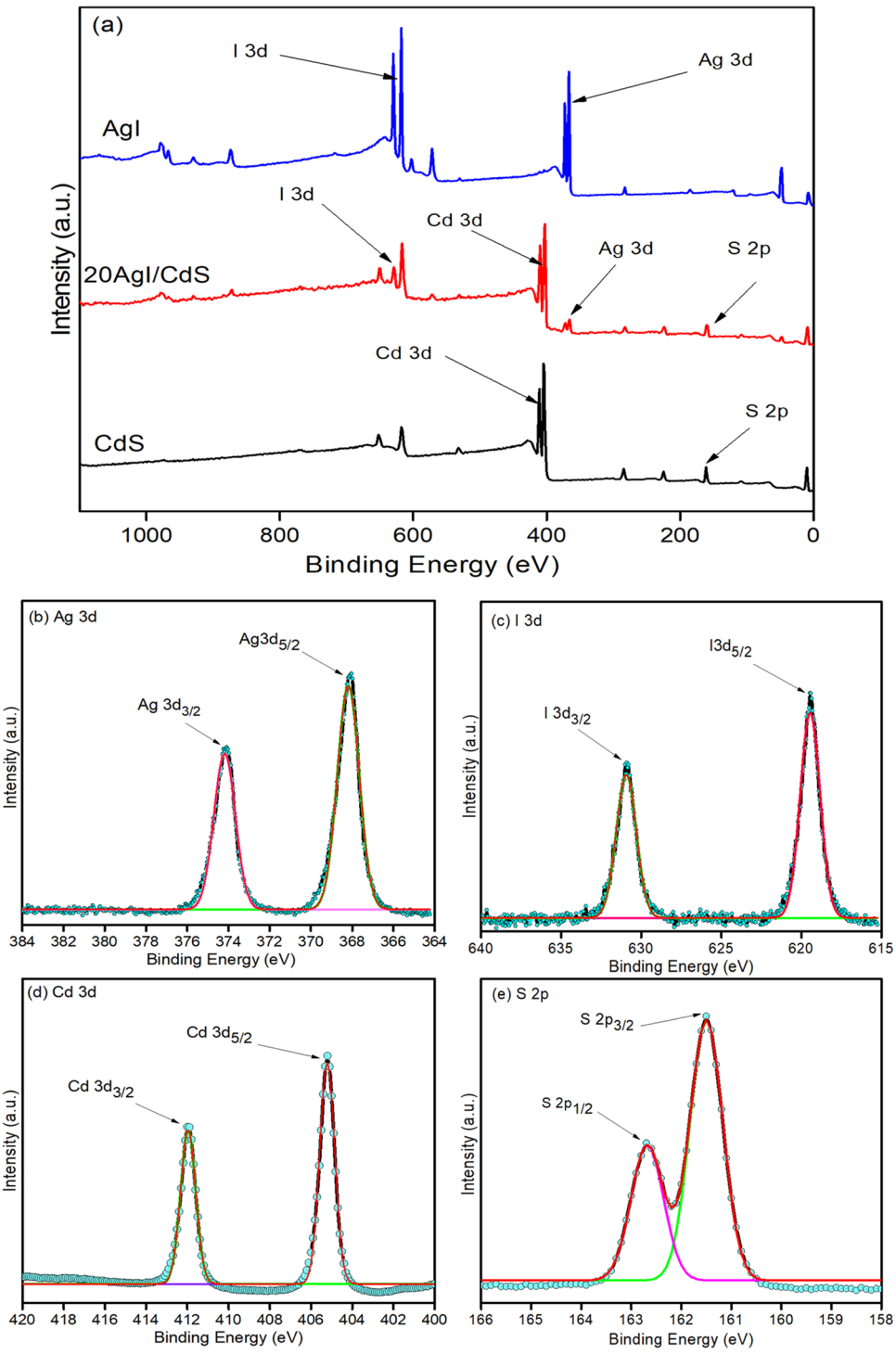

Figure 6. Survey scan XPS spectra of AgI, 20AgI/CdS, and CdS (a) and high-resolution spectra of Ag 3d (b), I 3d (c), Cd 3d (d), and S 2p (e) for 20CdS/AgI binary composite.

A controlled experiment was also carried out in the absence of the photocatalyst to validate that nearly no degradation of target molecules was seen. Figure 8a,b shows the decrease in peak intensity at 463 and 357 nm for MO and TCH in the presence of 20AgI/CdS binary composite as the visible light irradiation period increases. The depletion in concentrations of MO and TCH as a function of time in the presence of different pure and composite materials is depicted in Figure 8c,d. It was observed that the 20AgI/CdS binary composite exhibited the highest photocatalytic performances for MO and TCH degradation under the same conditions and irradiation times. When the AgI content in the CdS/AgI binary composite exceeded 20 weight percent, the photocatalytic performance declined. The reason for this might be that the substance contains an excessive amount of AgI particles, which might interact with the light and inhibit photocatalysts from absorbing as much of the radiation source as feasible. As shown in Figure 8c,d, pure AgI exhibits low photocatalytic activity for MO (43.8%) and TCH (47%) in 90 and 150 min of continuous irradiation, respectively. In the case of CdS,

https://doi.org/10.1021/acsomega.3c01517
ACS Omega 2023, 8, 22708−22720

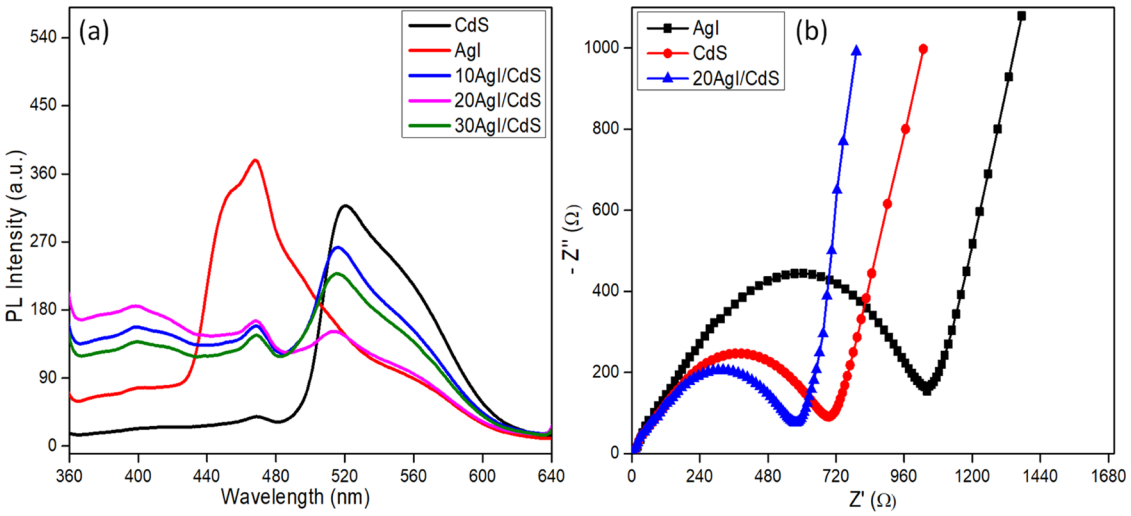

Figure 7. PL spectra of CdS, AgI, 10AgI/CdS, 20AgI/CdS, and 30AgI/CdS at an excitation wavelength of 330 nm (a) and EIS spectra of AgI, CdS, and 20AgI/CdS binary composite (b).

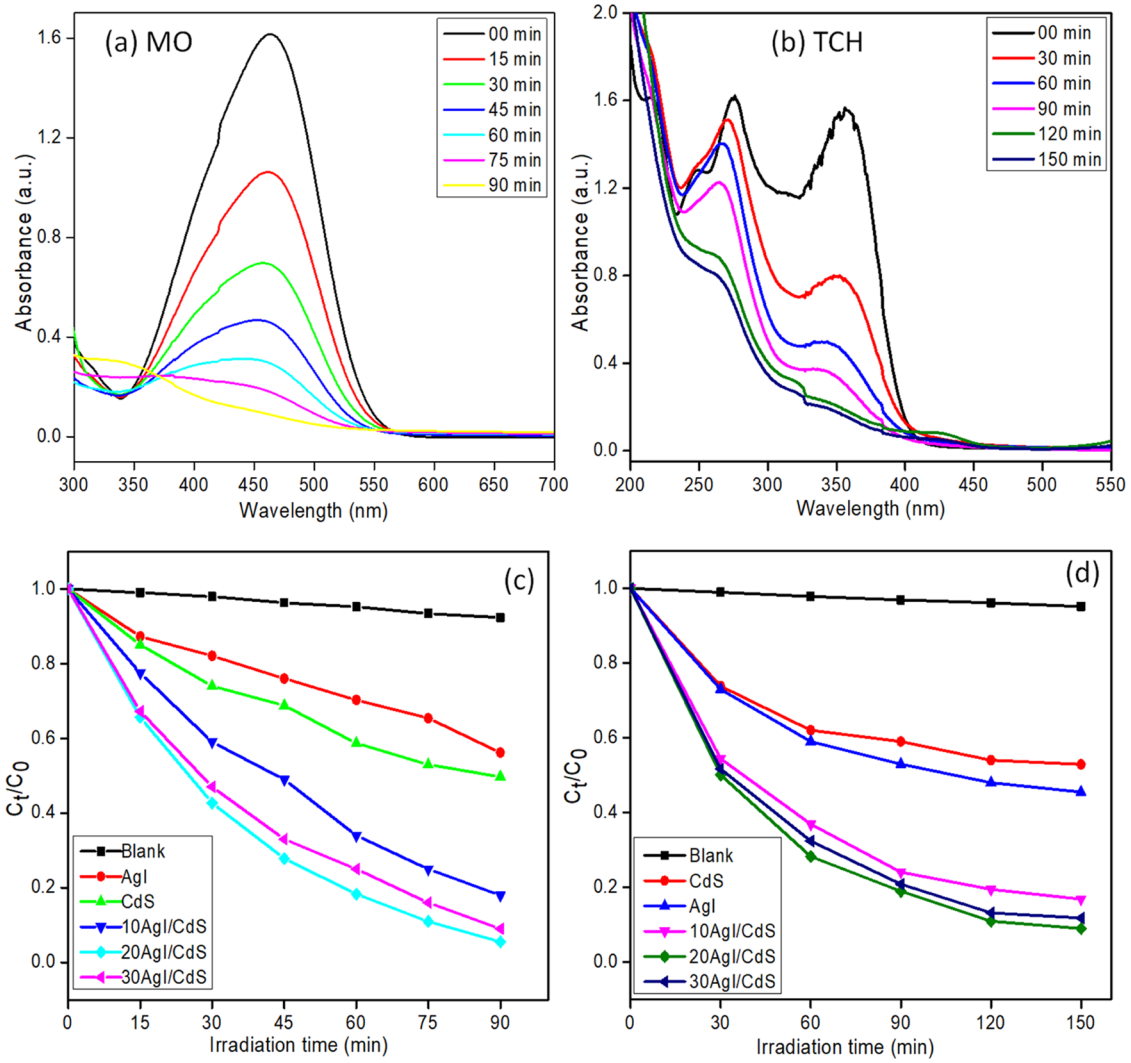

Figure 8. Changes in the absorbance of MO (a) and TCH (b) on irradiation over 20AgI/CdS binary composite at various time intervals; decrease in the concentrations of MO (c) and TCH (d) as a function of time in the absence and presence of various photocatalysts.

photocatalytic efficiency was found to be relatively high and about 50.3% of MO and 54.5% of TCH degraded. In contrast to bare AgI and CdS, all of the CdS/AgI binary composites significantly outperform them in photocatalytic abilities for

https://doi.org/10.1021/acsomega.3c01517
ACS Omega 2023, 8, 22708−22720

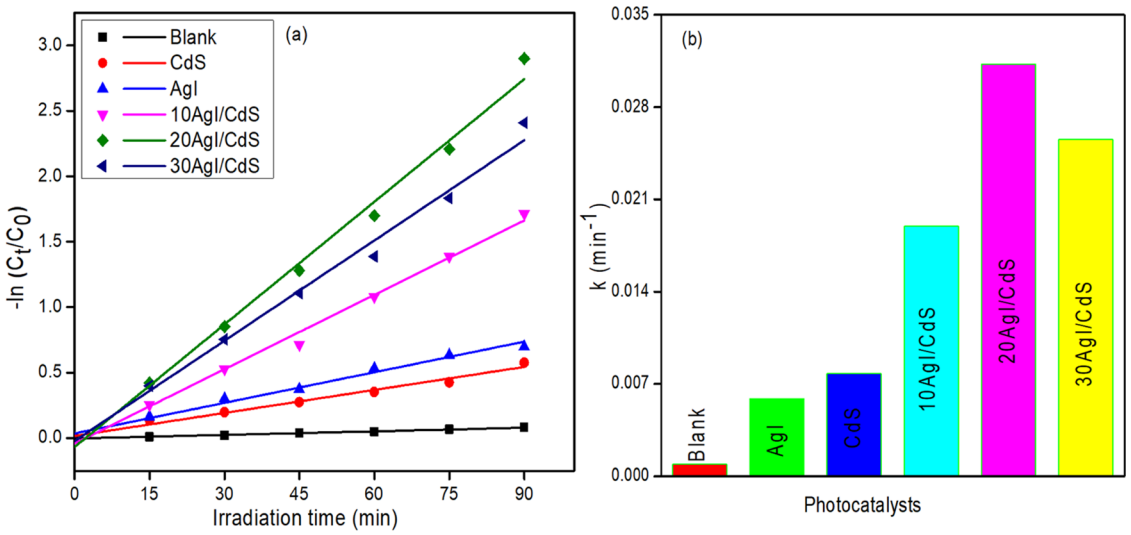

Figure 9. Plot of $-\ln C_t/C_0$ vs irradiation time for MO degradation kinetics in the absence and presence of different photocatalysts (a) and their corresponding rate constants (b).

MO and TCH degradations. The degradation efficiencies of optimized 20AgI/CdS binary composite for MO and TCH were found to be 94.5 and 91%, respectively. Synthesized materials, including pure and binary composites, degraded both organic pollutants in the following order: 20AgI/CdS > 30AgI/CdS > 10AgI/CdS > CdS > AgI.

The leaching of heavy metal (Cd) in the water from synthesized material during irradiation is of great concern. Therefore, the presence of Cd was checked by measuring concentration in the degraded sample of TCH using flame atomic absorption spectroscopy (AAS), and the result showed negligible presence of Cd metal (0.006 μg mL^{-1}).

To examine the intermediates generated and byproducts formed during the degradation of TCH and MO pollutants, high-performance liquid chromatography (HPLC) was employed. The HPLC chromatograms of irradiated samples of TCH and MO with binary composite (20AgI/CdS) under similar conditions are shown in Figures S3 and S4, respectively. The chromatogram illustrates that both starting compounds peak appearing at 03.72 and 4.03 min retention time (R_t) gradually decreases as illumination time increases. In addition, it is important to note here that in the case of TCH, there is a formation of intermediate product appearing at R_t 3.1 min for 60 and 90 min of irradiated samples, which on prolonged irradiation also decreased. The result indicates that both the starting compound and the intermediate formed during the photo-oxidation process are degraded. It is pertinent to mention here that the identification of intermediate products found during the photo-oxidation process of TCH using HPLC-MS has been reported earlier.[62,63]

2.8. Degradation Kinetics. The pseudo-first-order rate constants of the synthesized materials for MO degradation were determined by employing the Langmuir−Hinshelwood rate equation (eq 2).[64,65]

$$\ln(C_0/C_t) = k_{app}t \quad (2)$$

where k is the rate constant and C_0 and C_t are the starting and final concentrations at time t, respectively. Figure 9a shows the plot of $-\ln(C_0/C_t)$ vs irradiation time with linear fits for the degradation of MO with pure AgI, CdS, and AgI/CdS binary composites. The rate constants (k) obtained from these plots are presented in Figure 9b. For pure AgI, CdS, and binary composites (10AgI/CdS, 20AgI/CdS, and 30AgI/CdS), the obtained rate constant and associated correlation coefficients (R^2) are listed in Table 1. The apparent rate constants of the composite materials are greater than those of the pure materials, and optimized 20AgI/CdS displayed the highest among all the composites after 90 min of irradiation period. A slower reaction rate for photocatalytic degradation was observed with 30AgI/CdS compared to 20AgI/CdS binary composite. A further increase in AgI content may inhibit the light absorption capacity of the 30AgI/CdS binary composite, and as a result decreased in the photodegradation was observed.

Table 1. Pseudo-First-Order Rate Constant and the Corresponding R^2 Values for Blank, CdS, AgI, 10AgI/CdS, 20AgI/CdS, and 30AgI/CdS Involved in the Photocatalytic Degradation of MO

sample	apparent rate constant, k (min^{-1})	R^2
blank	0.000913	0.9918
CdS	0.00586	0.98027
AgI	0.00779	0.98438
10AgI/CdS	0.01895	0.99243
20AgI/CdS	0.03124	0.9904
30AgI/CdS	0.02554	0.98882

2.9. Reusability and Stability. Reusability and stability are two crucial aspects that play a major role in determining the practical application of these catalysts. Recycling experiments for the degradation of MO over the 20AgI/CdS composite under simulated solar light irradiation were carried out for three consecutive runs, and the results are displayed in Figure 10a. After each irradiation, the catalyst was centrifuged, washed, dried, and used for the next irradiation experiments. After three successive rounds of repetitive photocatalytic activity testing, the composite material showed exceptional stability and recyclability. The XRD patterns of the irradiated sample were recorded and compared with those of the unirradiated sample, as shown in Figure 10b. The diffraction pattern of irradiated sample was found to be unaltered,

https://doi.org/10.1021/acsomega.3c01517
ACS Omega 2023, 8, 22708−22720

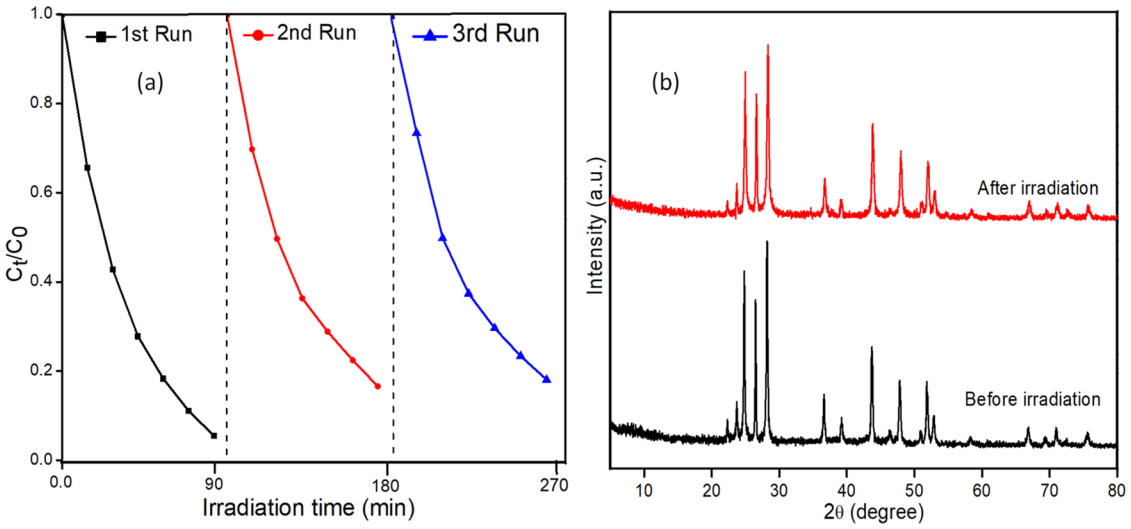

Figure 10. Recyclability experiment of 20AgI/CdS binary composite in the photocatalytic degradation of MO for three repetitive cycles (a); XRD patterns of 20AgI/CdS binary composite before and after irradiation (b).

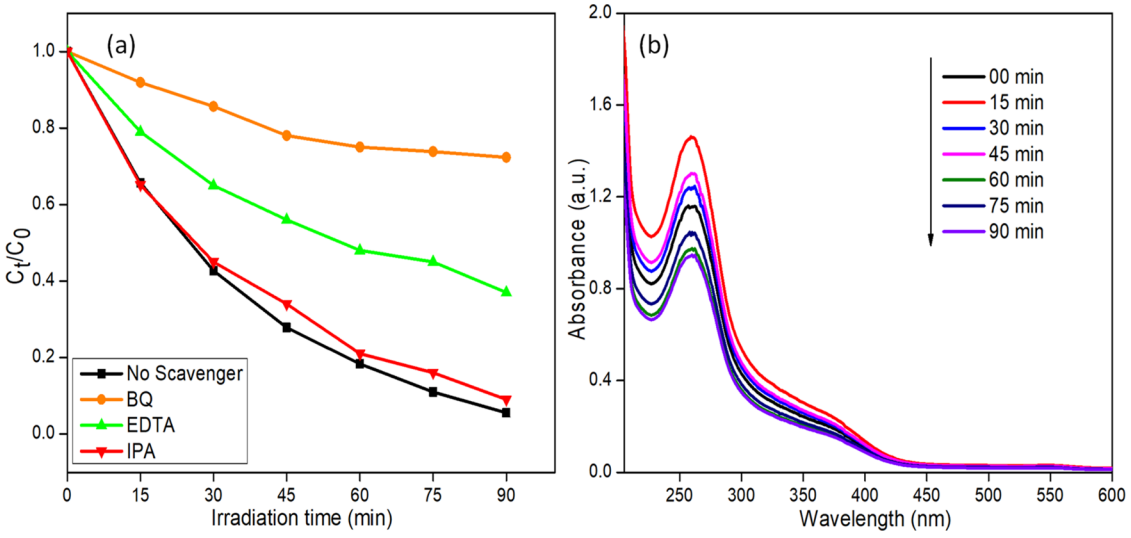

Figure 11. Change in the concentrations of MO as a function of time in the absence and presence of various scavengers using the 20AgI/CdS binary composite (a); UV−vis absorption spectral changes of NBT over 20AgI/CdS in different time intervals (b).

although it has been reported in the literature that AgI decomposes to form Ag^0 species as a result of photoreduction during irradiation processes.[66] However, in the present study, Ag^0 peaks were not clearly visible in the XRD pattern due to the low content of AgI. A slight decrease in the peak intensity of the used catalyst was also observed. As per our findings, the 20AgI/CdS binary composite is sufficiently stable during the photodegradation of the MO and may be reused repeatedly without suffering a significant performance decline.

2.10. Active Species Trapping Experiments and Photocatalytic Mechanism. Trapping experiments were conducted to determine the dominating active species by studying the degradation of MO in the absence and presence of different quenchers, and the results are shown in Figure 11a. Generally, reactive species like superoxide radicals ($O_2^{\bullet-}$), holes (h^+), and hydroxyl radicals ($^\bullet OH$) radicals are involved in photocatalytic oxidation processes to degrade the toxic organic pollutants.[67] The quenchers such as isopropyl alcohol (IPA),[68,69] ethylenediamine tetraacetic acid disodium (EDTA-2Na),[70,71] and benzoquinone (BQ)[72,73] were used to trap the $^\bullet OH$, h^+, and $O_2^{\bullet-}$, respectively. These reactive species were generated during the photodegradation processes in the MO and AgI/CdS binary composite reaction mixture. The photocatalytic degradation was almost 94.5% when no quencher was added. The addition of IPA has no noticeable impact, demonstrating that $^\bullet OH$ radicals play no significant role in photodegradation. The addition of BQ to the reaction mixture dramatically dropped the MO degradation from 94.5 to 23%, demonstrating that $O_2^{\bullet-}$ was the most significant reactive species found in the reaction mixture. By contrast, adding EDTA-2Na reduced MO degradation to 60%, suggesting that h^+ participated in photodegradation synergistically but to a lesser extent than the $O_2^{\bullet-}$. Besides this, an NBT transformation experiment using 20AgI/CdS binary composite was performed to confirm the generation of $O_2^\bullet$ further, and the results are shown in Figure 11b. The gradual reduction in the absorption peak intensity at 260 nm of NBT confirms the participation of $O_2^{\bullet-}$ as a significant reactive species.

Regarding photocatalytic degradation processes, the valence band (VB) and conduction band (CB) edge potentials of

https://doi.org/10.1021/acsomega.3c01517
ACS Omega 2023, 8, 22708−22720

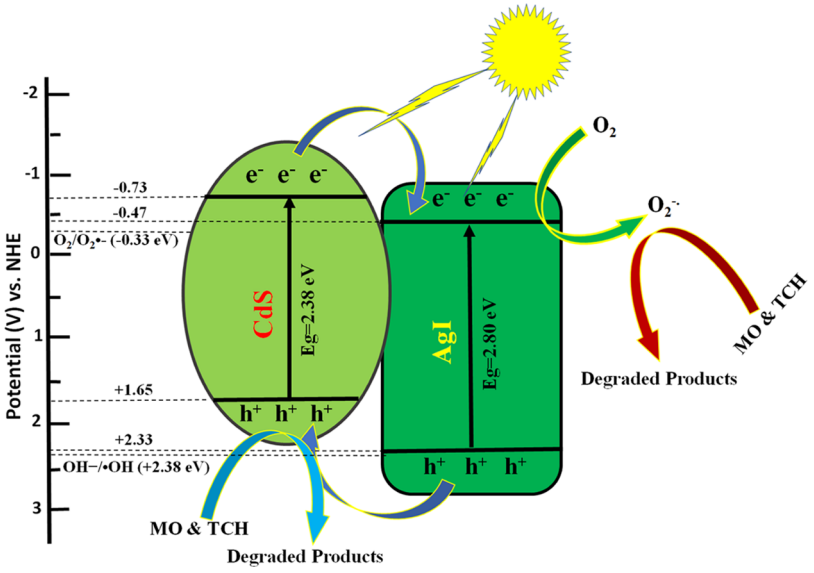

Figure 12. Schematic illustration of a type-II mechanism for MO and TCH degradation by the CdS/AgI binary composite under visible light illumination.

semiconductor materials are of utmost importance. It is worth noting that the driving force behind charge transfer is typically derived from the compatible band potentials of the two semiconductors. Therefore, the potentials at the band edges of the synthesized materials were determined using eqs 3 and 4.[74]

$$E_{VB} = X - E^{e} + \frac{1}{2} E_{g} \quad (3)$$

$$E_{CB} = E_{VB} - E_{g} \quad (4)$$

where different parameters are E_{VB} and E_{CB} (VB and CB edge potentials), X (absolute electronegativity of the semiconductor), E^{e} {energy of the free electron (4.5 eV) against NHE}, and E_{g} (optical bandgap energy in eV). The calculated conduction band (CB) and valence band (VB) potentials of CdS are −0.73 and +1.65 eV, while the CB and VB potentials of AgI are estimated to be −0.47 and 2.33 eV, respectively. In addition, the calculated E_{VB} values are in agreement with the valence band (VB) XPS spectra of CdS and AgI, as shown in Figure S2a,b. Due to the rapid recombination of the charge carriers, these semiconductor materials in their pure form typically result in poor photodegradation efficiency. However, the band edge positions of CdS and AgI are so well matched in the CdS/AgI binary composite that photoinduced charge carriers can easily be transferred between the two semiconductors. A scheme for the separation and transport of photogenerated charges at the interface of CdS/AgI binary composite is depicted in Figure 12. Both AgI and CdS are capable of being excited by visible light, resulting in the generation of photogenerated electrons and holes. The electrons excited on the CB of CdS can directly transfer to the CB of AgI, which has a more negative redox potential (−0.47) than the standard redox potential of $O_2/O_2^{\bullet-}$ (−0.33 eV vs NHE).[75] As a result, the electrons present in the CB of AgI can react with O_2 to produce $O_2^{\bullet-}$. When irradiated, Ag^+ is reduced to Ag^0, which can then be excited to release electrons and react with O_2 to form $O_2^{\bullet-}$.[76] These generated $O_2^{\bullet-}$ then interacted with the organic pollutants and degraded them into harmless substances. At the same time, the holes created in the VB of AgI transferred to the VB of CdS, where it directly reacted with the pollutants. Since the redox potential of CdS (+1.65) is less positive than the $^{\bullet}OH/OH^-$ potential (+2.38 eV vs NHE) and the $H_2O/^{\bullet}OH$ (+2.72 eV vs NHE), the holes are unable to convert the OH^- and H_2O into $^{\bullet}OH$.[40,77] The following reactions can be given as a concise summary of all of the processes that are involved in degradation pathways (eqs 5−8)

$$CdS/AgI + h\nu \rightarrow CdS/AgI\ (e^- + h^+) \quad (5)$$

$$O_2 + e^- \rightarrow O_2^{\bullet-} \quad (6)$$

$$MO + O_2^{\bullet-},\ h^+ \rightarrow \text{degradation products} \quad (7)$$

$$TC + O_2^{\bullet-},\ h^+ \rightarrow \text{degradation products} \quad (8)$$

3. CONCLUSIONS

A novel binary composite (CdS/AgI) has been synthesized using the *in situ* precipitation method and characterized by XRD, SEM, EDX mapping, HRTEM, XPS, UV−vis DRS, and FT-IR analyses. When exposed to visible light, the prepared synthesized materials quickly and efficiently degraded the MO and TCH pollutants in an aqueous suspension. The significantly enhanced photocatalytic activity of the binary composite was primarily attributed to the abundance of active sites and the effective separation rate of photogenerated charge carriers resulting from well-matched band potentials. The PL analysis showed that the 20AgI/CdS binary composite possessed the highest charge carrier separation efficiency. The findings of the scavenger experiments revealed that $O_2^{\bullet-}$ was the primary active species responsible for the degradation of MO and TCH over the CdS/AgI binary composites. Three consecutive photocatalytic experiments utilizing the same photocatalyst revealed that the 20AgI/CdS binary composite exhibited remarkable stability. The findings of the study suggest that CdS/AgI might be a feasible option for the treatment of organic dyes and antibiotics present in wastewater bodies.

https://doi.org/10.1021/acsomega.3c01517
ACS Omega 2023, 8, 22708−22720

4. EXPERIMENTAL SECTION

4.1. Synthesis of Pure CdS. The CdS photocatalyst was synthesized using the solvothermal method.[78] 5 mmol of $Cd(NO_3)_2{\cdot}4H_2O$ was dissolved in 35 mL of ethylenediamine (EDA), and the solution was then stirred for 1 h. Thereafter, 15 mmol of thiourea was added to the EDA solution and thoroughly mixed until a clear solution appeared. Finally, the entire content was heated for 56 h at 180 °C in a stainless-steel autoclave lined with Teflon. The material was filtered and washed with water and ethanol. The obtained yellow product was then dried overnight at 120 °C.

4.2. Synthesis of CdS/AgI Binary Composite. A series of CdS/AgI photocatalysts were synthesized by an *in situ* precipitation method, and the steps involved are shown in Scheme S1. The three separate solutions of 85, 170, and 255 mg of $AgNO_3$ were prepared in 30 mL of water and the solutions were named as A, B, and C, in which 83, 166, and 249 mg of KI was added slowly with stirring. After 30 min of constant stirring, a light-yellow-colored precipitate was obtained. An equal amount of CdS (1.17 g) was added to the above solutions and sonicated for 90 min. The obtained residue was filtered and washed with ethanol and water before being dried at 120 °C for 12 h. The powdered material obtained from solutions A, B, and C were marked as 10AgI/CdS, 20AgI/CdS, and 30AgI/CdS (where 10, 20, and 30 are the percent mass ratios of AgI to CdS/AgI), respectively. Pure AgI was also synthesized using the same method without adding CdS.

■ ASSOCIATED CONTENT

Supporting Information

The Supporting Information is available free of charge at https://pubs.acs.org/doi/10.1021/acsomega.3c01517.

High-resolution XPS spectra of Ag 3d, I 3d, Cd 3d, and S 2p for pure photocatalysts and 20AgI/CdS binary composites (Figure S1); valence band (VB) XPS spectra of CdS and AgI (Figure S2); HPLC chromatograms of TCH (Figure S3) and MO (Figure S4); synthetic procedure for CdS/AgI binary composite (Scheme S1); details of chemicals required (Section S4.3), materials characterization techniques (Section S4.4); process for measurement of photocatalytic activity (Section S4.5) and setup for photocatalytic reaction showing immersion well photoreactor (Figure S5); and requirements for trapping studies (Section S4.6) (PDF)

■ AUTHOR INFORMATION

Corresponding Authors

Mohammad Muneer − *Department of Chemistry, Aligarh Muslim University, Aligarh 202002, India;* orcid.org/0009-0004-7899-0478; Email: m.muneer.ch@amu.ac.in

Saleh A. Ahmed − *Department of Chemistry, Faculty of Applied Sciences, Umm Al-Qura University, Makkah 21955, Saudi Arabia*; Email: saahmed@uqu.edu.sa

Authors

Iftekhar Ahmad − *Department of Chemistry, Aligarh Muslim University, Aligarh 202002, India*

Abdelrahman S. Khder − *Department of Chemistry, Faculty of Applied Sciences, Umm Al-Qura University, Makkah 21955, Saudi Arabia;* orcid.org/0000-0002-4886-6116

Complete contact information is available at: https://pubs.acs.org/10.1021/acsomega.3c01517

Notes

The authors declare no competing financial interest.

■ ACKNOWLEDGMENTS

The authors extend their appreciation to the Deputyship for Research & Innovation, Ministry of Education in Saudi Arabia for funding this research work through the project number: IFP22UQU4320545DSR110. The authors acknowledge the DST and UGC for DRS II, PURSE & FIST to the Department of Chemistry, Aligarh Muslim University, Aligarh. Iftekhar Ahmad is highly thankful to UGC-CSIR, New Delhi, India, for the Senior Research Fellowship (SRF) award.

■ REFERENCES

(1) Wang, Q.; Li, Y.; Huang, L.; Zhang, F.; Wang, H.; Wang, C.; Zhang, Y.; Xie, M.; Li, H. Enhanced Photocatalytic Degradation and Antibacterial Performance by GO/CN/BiOI Composites under LED Light. *Appl. Surf. Sci.* **2019**, *497*, No. 143753.

(2) Talebzadeh, Z.; Masjedi-Arani, M.; Amiri, O.; Salavati-Niasari, M. $La_2Sn_2O_7$/g-C_3N_4 Nanocomposites: Rapid and Green Sonochemical Fabrication and Photo-Degradation Performance for Removal of Dye Contaminations. *Ultrason. Sonochem.* **2021**, *77*, No. 105678.

(3) Nefzi, C.; Askri, B.; Yahmadi, B.; El Guesmi, N.; García, J. M.; Kamoun-Turki, N.; Ahmed, S. A. Competence of Tunable Cu_2AlSnS_4 Chalcogenides Hydrophilicity toward High Efficacy Photodegradation of Spiramycin Antibiotic Resistance-Bacteria from Wastewater under Visible Light Irradiation. *J. Photochem. Photobiol. A* **2022**, *431*, No. 114041.

(4) Seddigi, Z.; Saleh, S.; Ansari, S. P. Method of Photocatalytic Degradation of Contaminant in Water Using Visible Light Source. U.S. Patent US9,403,696, 2016.

(5) Sun, Y.; Zhu, Q.; Bai, B.; Li, Y.; He, C. Novel All-Solid-State Z-Scheme SnO_2/Pt/In_2O_3 Photocatalyst with Boosted Photocatalytic Performance on Water Splitting and 2,4-Dichlorophenol Degradation under Visible Light. *Chem. Eng. J.* **2020**, *390*, No. 124518.

(6) Athar, M. S.; Muneer, M. Enhanced Photodegradation of Organic Contaminants Using V-ZnSQDs@TiO_2 Photocatalyst in an Aqueous Medium. *Photochem. Photobiol. Sci.* **2023**, *22*, 695−712.

(7) Ansari, M. A.; Albetran, H. M.; Alheshibri, M. H.; Timoumi, A.; Algarou, N. A.; Akhtar, S.; Slimani, Y.; Almessiere, M. A.; Alahmari, F. S.; Baykal, A.; Low, I. M. Synthesis of Electrospun TiO_2 Nanofibers and Characterization of Their Antibacterial and Antibiofilm Potential against Gram-Positive and Gram-Negative Bacteria. *Antibiotics* **2020**, *9*, 572.

(8) Lakhera, S. K.; Hafeez, H. Y.; Veluswamy, P.; Ganesh, V.; Khan, A.; Ikeda, H.; Neppolian, B. Enhanced Photocatalytic Degradation and Hydrogen Production Activity of in Situ Grown TiO_2 Coupled $NiTiO_3$ Nanocomposites. *Appl. Surf. Sci.* **2018**, *449*, 790−798.

(9) Jiang, L.; Yuan, X.; Zeng, G.; Liang, J.; Chen, X.; Yu, H.; Wang, H.; Wu, Z.; Zhang, J.; Xiong, T. In-Situ Synthesis of Direct Solid-State Dual Z-Scheme WO_3/g-C_3N_4/Bi_2O_3 Photocatalyst for the Degradation of Refractory Pollutant. *Appl. Catal., B* **2018**, *227*, 376−385.

(10) Mohamed, M. M.; Osman, G.; Khairou, K. S. Fabrication of Ag Nanoparticles Modified TiO_2-CNT Heterostructures for Enhanced Visible Light Photocatalytic Degradation of Organic Pollutants and Bacteria. *J. Environ. Chem. Eng.* **2015**, *3*, 1847−1859.

(11) Li, J.; Tang, Y.; Jin, R.; Meng, Q.; Chen, Y.; Long, X.; Wang, L.; Guo, H.; Zhang, S. Ultrasonic-Microwave Assisted Synthesis of GO/g-C_3N_4 Composites for Efficient Photocatalytic H2 Evolution. *Solid State Sci.* **2019**, *97*, No. 105990.

(12) Liu, B.; Mu, L.; Han, X.; Zhang, J.; Shi, H. Highly Efficient Visible-Light-Driven Photocatalytic Activity of g-C_3N_4@Ag/$AgVO_3$ Composites for Dye Degradation and Bacterial Inactivation. *J. Photochem. Photobiol. A* **2019**, *380*, No. 111866.

(13) Abubshait, H. A.; Saad, M.; Iqbal, S.; Abubshait, S. A.; Bahadur, A.; Raheel, M.; Alshammari, F. H.; Alwadai, N.; Alrbyawi, H.; Abourehab, M. A. S.; Elkaeed, E. B.; Qayyum, M. A.; Somaily, H. H. Co-Doped Zinc Oxide Nanoparticles Embedded in Polyvinylalcohol Hydrogel as Solar Light Derived Photocatalyst Disinfection and Removal of Coloured Pollutants. *J. Mol. Struct.* **2023**, *1271*, No. 134100.
(14) Bawazeer, T. M.; Alsoufi, M. S.; Shkir, M.; Al-Shehri, B. M.; Hamdy, M. S. Excellent Improvement in Photocatalytic Nature of ZnO Nanoparticles via Fe Doping Content. *Inorg. Chem. Commun.* **2021**, *130*, No. 108668.
(15) Sun, N.; Zhu, Y.; Li, M.; Zhang, J.; Qin, J.; Li, Y.; Wang, C. Thermal Coupled Photocatalysis over Pt/g-C_3N_4 for Selectively Reducing CO_2 to CH_4 via Cooperation of the Electronic Metal−Support Interaction Effect and the Oxidation State of Pt. *Appl. Catal., B* **2021**, *298*, No. 120565.
(16) Wang, M.; Zhang, Y.; Jin, C.; Li, Z.; Chai, T.; Zhu, T. Fabrication of Novel Ternary Heterojunctions of Pd/g-C_3N_4/Bi_2MoO_6 Hollow Microspheres for Enhanced Visible-Light Photocatalytic Performance toward Organic Pollutant Degradation. *Sep. Purif. Technol.* **2019**, *211*, 1−9.
(17) Seddigi, Z.; Saleh, S. A. Process of Using a Catalyst for Photo-Catalytic Degradation of Contaminant in Water. U.S. Patent US9,339,795, 2016.
(18) Xie, R.; Fang, K.; Liu, Y.; Chen, W.; Fan, J.; Wang, X.; Ren, Y.; Song, Y. Z-Scheme In_2O_3/WO_3 Heterogeneous Photocatalysts with Enhanced Visible-Light-Driven Photocatalytic Activity toward Degradation of Organic Dyes. *J. Mater. Sci.* **2020**, *55*, 11919−11937.
(19) Wannakan, K.; Khansamrit, K.; Senasu, T.; Nanan, S. Ultrasound-Assisted Synthesis of a ZnO/$BiVO_4$ S-Scheme Heterojunction Photocatalyst for Degradation of the Reactive Red 141 Dye and Oxytetracycline Antibiotic. *ACS Omega* **2023**, *8*, 4835−4852.
(20) Dineshbabu, N.; Jayaprakash, R. N.; Karuppasamy, P.; Arun, T.; Vijaya, J. J.; Nimshi, R. E.; Pandian, M. S.; Packiam, S. M.; Ramasamy, P. Investigation on Tetracycline Degradation and Bactericidal Properties of Binary and Ternary ZnO/NiO/g-C_3N_4 Composites Prepared by a Facile Co-Precipitation Method. *J. Environ. Chem. Eng.* **2022**, *10*, No. 107368.
(21) Ali, H. R.; Motawea, E. A. Ternary Photodegradable Nanocomposite (BiOBr/ZnO/WO_3) for the Degradation of Phenol Pollutants: Optimization and Experimental Design. *ACS Omega* **2021**, *6*, 22047−22064.
(22) Li, K.; Chen, J.; Ao, Y.; Wang, P. Preparation of a Ternary G-C_3N_4-CdS/$Bi_4O_5I_2$ Composite Photocatalysts with Two Charge Transfer Pathways for Efficient Degradation of Acetaminophen under Visible Light Irradiation. *Sep. Purif. Technol.* **2021**, *259*, No. 118177.
(23) Qiu, H.; Li, F.; He, S.; Shi, R.; Han, Y.; Abudukeremu, H.; Zhang, L.; Zhang, Y.; Wang, S.; Liu, W.; Ma, C.; Fang, H.; Long, R.; et al. Epitaxial CsPbBr3/CdS Janus Nanocrystal Heterostructures for Efficient Charge Separation. *Adv. Sci.* **2023**, *10*, No. e2206560.
(24) Wang, D.; Shen, H.; Guo, L.; Fu, F.; Liang, Y. Design and Construction of the Sandwich-like Z-Scheme Multicomponent CdS/Ag/Bi_2MoO_6 Heterostructure with Enhanced Photocatalytic Performance in RhB Photodegradation. *New J. Chem.* **2016**, *40*, 8614−8624.
(25) Liu, Y.; Wang, H.; Yuan, X.; Wu, Y.; Wang, H.; Tan, Y. Z. Review Roles of Sulfur-Edge Sites, Metal-Edge Sites, Terrace Sites, and Defects in Metal Sulfides for Photocatalysis. *Chem Catal.* **2021**, *1*, 44−68.
(26) Mirsalari, S. A.; Nezamzadeh-Ejhieh, A. CdS−Ag_3PO_4 Nano-Catalyst: A Brief Characterization and Kinetic Study towards Methylene Blue Photodegradation. *Mater. Sci. Semicond. Process.* **2021**, *122*, No. 105455.
(27) Nasir, J. A.; Rehman, Z.; Catlow, C. R. A.; et al. Recent Developments and Perspectives in CdS-Based Photocatalysts for Water Splitting. *J. Mater. Chem. A* **2020**, *8*, 20752−20780.
(28) Shao, B.; Liu, X.; Liu, Z.; Zeng, G.; Zhang, W.; Liang, Q.; Liu, Y.; He, Q.; Yuan, X.; Wang, D.; Luo, S.; Gong, S. Synthesis and Characterization of 2D/0D g-C_3N_4/CdS-Nitrogen Doped Hollow Carbon Spheres (NHCs)Composites with Enhanced Visible Light Photodegradation Activity for Antibiotic. *Chem. Eng. J.* **2019**, *374*, 479−493.
(29) El-Katori, E. E.; Ahmed, M. A.; El-Bindary, A. A.; Oraby, A. M. Impact of CdS/SnO_2 heterostructured Nanoparticle as Visible Light Active Photocatalyst for the Removal Methylene Blue Dye. *J. Photochem. Photobiol. A* **2020**, *392*, No. 112403.
(30) Tong, M.; Sun, D.; Zhang, R.; Liu, H.; Chen, R. Preparation of Si−α-Fe_2O_3/CdS Composites with Enhanced Visible-Light Photocatalytic Activity for p-Nitrophenol Degradation. *J. Alloys Compd.* **2021**, *862*, No. 158271.
(31) Zhang, C.; Liu, B.; Li, W.; Liu, X.; Wang, K.; Deng, Y.; Guo, Z.; Lv, Z. A Well-Designed Honeycomb Co_3O_4@CdS Photocatalyst Derived from Cobalt Foam for High-Efficiency Visible-Light H_2 evolution. *J. Mater. Chem. A* **2021**, *9*, 11665−11673.
(32) Zhang, C.; Liu, B.; Cheng, X.; Guo, Z. M.; Zhuang, T.; Lv, Z. A CdS@NiS Reinforced Concrete Structure Derived from Nickel Foam for Efficient Visible-Light H_2 Production. *Chem. Eng. J.* **2020**, *393*, No. 124774.
(33) Duan, Y.; Deng, L.; Shi, Z.; Zhu, L.; Li, G. Assembly of Graphene on Ag_3PO_4/AgI for Effective Degradation of Carbamazepine under Visible-Light Irradiation: Mechanism and Degradation Pathways. *Chem. Eng. J.* **2019**, *359*, 1379−1390.
(34) Guan, D. L.; Niu, C. G.; Wen, X. J.; Guo, H.; Deng, C. H.; Zeng, G. M. Enhanced Escherichia Coli Inactivation and Oxytetracycline Hydrochloride Degradation by a Z-Scheme Silver Iodide Decorated Bismuth Vanadate Nanocomposite under Visible Light Irradiation. *J. Colloid Interface Sci.* **2018**, *512*, 272−281.
(35) Pourshirband, N.; Nezamzadeh-Ejhieh, A.; Mirsattari, S. N. The CdS/g-C_3N_4 Nano-Photocatalyst: Brief Characterization and Kinetic Study of Photodegradation and Mineralization of Methyl Orange. *Spectrochim. Acta, Part A* **2021**, *248*, No. 119110.
(36) Li, N.; DIng, Y.; Wu, J.; Zhao, Z.; Li, X.; Zheng, Y. Z.; Huang, M.; Tao, X. Efficient, Full Spectrum-Driven H2 Evolution Z-Scheme Co_2P/CdS Photocatalysts with Co-S Bonds. *ACS Appl. Mater. Interfaces* **2019**, *11*, 22297−22306.
(37) Li, X.; Wu, D.; Luo, Q.; An, J.; Yin, R.; Wang, D. Advanced Cyclized Polyacrylonitrile (CPAN)/CdS Nanocomposites for Highly Efficient Visible-Light Photocatalysis. *J. Mater. Sci.* **2017**, *52*, 736−748.
(38) Salesi, S.; Nezamzadeh-Ejhieh, A. Boosted Photocatalytic Effect of Binary AgI/Ag_2WO_4 Nanocatalyst: Characterization and Kinetics Study towards Ceftriaxone Photodegradation. *Environ. Sci. Pollut. Res.* **2022**, *29*, 90191−90206.
(39) Reddy, D. A.; Choi, J.; Lee, S.; Ma, R.; Kim, T. K. Green Synthesis of AgI Nanoparticle-Functionalized Reduced Graphene Oxide Aerogels with Enhanced Catalytic Performance and Facile Recycling. *RSC Adv.* **2015**, *5*, 67394−67404.
(40) Xue, W.; Huang, D.; Li, J.; Zeng, G.; Deng, R.; Yang, Y.; Chen, S.; Li, Z.; Gong, X.; Li, B. Assembly of AgI Nanoparticles and Ultrathin G-C_3N_4 Nanosheets Codecorated Bi_2WO_6 Direct Dual Z-Scheme Photocatalyst: An Efficient, Sustainable and Heterogeneous Catalyst with Enhanced Photocatalytic Performance. *Chem. Eng. J.* **2019**, *373*, 1144−1157.
(41) Wang, Y.; Chen, J.; Liu, L.; Xi, X.; Li, Y.; Geng, Z.; Jiang, G.; Zhao, Z. Novel Metal Doped Carbon Quantum Dots/CdS Composites for Efficient Photocatalytic Hydrogen Evolution. *Nanoscale* **2019**, *11*, 1618−1625.
(42) Huang, S.; Zhang, J.; Qin, Y.; Song, F.; Du, C.; Su, Y. Direct Z-Scheme SnO_2/$Bi_2Sn_2O_7$ Photocatalyst for Antibiotics Removal: Insight on the Enhanced Photocatalytic Performance and Promoted Charge Separation Mechanism. *J. Photochem. Photobiol. A* **2021**, *404*, No. 112947.
(43) Nefzi, C.; Yahmadi, B.; Guesmi, N.; El García, J. M.; Kamoun-Turki, N.; Ahmed, S. A. A Successful Exploitation of Gamma-Radiation on Chalcogenide Cu_2InSnS_4 towards Clean Water under Photocatalysis Approach. *J. Mol. Struct.* **2022**, *1251*, No. 131943.
(44) Wu, S.; Wang, Y. Construction of C@WS_2/g-C_3N_4 Z-Scheme Photocatalyst with C Film as an Effective Electron Mediator and Its

https://doi.org/10.1021/acsomega.3c01517
ACS Omega 2023, 8, 22708−22720

Enhanced Degradation of 2,4-Dichlorophenol under Visible Light. *Chemosphere* **2021**, *273*, No. 129746.
(45) Singh, S.; Atri, A. K.; Qadir, I.; Sharma, S.; Manhas, U.; Singh, D. Role of Different Fuels and Sintering Temperatures in the Structural, Optical, Magnetic, and Photocatalytic Properties of Chromium- Containing Nickel Ferrite: Kinetic Study of Photocatalytic Degradation of Rhodamine B Dye. *ACS Omega* **2023**, *8*, 6302−6317.
(46) Wang, T.; Quan, W.; Jiang, D.; Chen, L.; Li, D.; Meng, S.; Chen, M. Synthesis of Redox-Mediator-Free Direct Z-Scheme AgI/WO_3 Nanocomposite Photocatalysts for the Degradation of Tetracycline with Enhanced Photocatalytic Activity. *Chem. Eng. J.* **2016**, *300*, 280−290.
(47) Feng, Y.; Yan, X.; Liu, C.; Hong, Y.; Zhu, L.; Zhou, M.; Shi, W. Hydrothermal Synthesis of CdS/Bi_2MoO_6 Heterojunction Photocatalysts with Excellent Visible-Light-Driven Photocatalytic Performance. *Appl. Surf. Sci.* **2015**, *353*, 87−94.
(48) Yu, H.; Yin, H.; Wang, L.; Gong, J.; Zheng, Y.; Nie, Q. Enhanced Degradation of Rhodamine B, Tetracycline and Carbamazepine by Construction of a Solar Driven Indirect Z-Scheme AgI/Ag/$Bi_2O_2CO_3$ Nanosheets Photocatalyst. *J. Mater. Sci. Mater. Electron.* **2019**, *30*, 17227−17238.
(49) Zhou, X.; Chen, Y.; Wang, P.; Xu, C.; Yan, Q. Fabrication of AgI/$BiPO_4$ n−n Heterojunction Photocatalyst for Efficient Degradation of Organic Pollutants. *J. Mater. Sci. Mater. Electron.* **2020**, *31*, 12638−12648.
(50) Zhang, G.; Chen, D.; Li, N.; Xu, Q.; Li, H.; He, J.; Lu, J. Preparation of $ZnIn_2S_4$ Nanosheet-Coated CdS Nanorod Heterostructures for Efficient Photocatalytic Reduction of Cr(VI). *Appl. Catal., B* **2018**, *232*, 164−174.
(51) Huang, H.; Li, Y. X.; Wang, H. L.; Jiang, W. F. In Situ Fabrication of Ultrathin-g-C_3N_4/AgI Heterojunctions with Improved Catalytic Performance for Photodegrading Rhodamine B Solution. *Appl. Surf. Sci.* **2021**, *538*, No. 148132.
(52) Vosoughi, F.; Habibi-Yangjeh, A.; Asadzadeh-Khaneghah, S.; Ghosh, S.; Maiyalagan, T. Novel Ternary G-C_3N_4 Nanosheet/Ag_2MoO_4/AgI Photocatalysts: Impressive Photocatalysts for Removal of Various Contaminants. *J. Photochem. Photobiol. A* **2020**, *403*, No. 112871.
(53) Shoja, A.; Habibi-Yangjeh, A.; Mousavi, M.; Vadivel, S. Preparation of Novel Ternary TiO_2 QDs/CDs/AgI Nanocomposites with Superior Visible-Light Induced Photocatalytic Activity. *J. Photochem. Photobiol. A* **2019**, *385*, No. 112070.
(54) Gupta, R.; Eswar, N. K. R.; Modak, J. M.; Madras, G. Effect of Morphology of Zinc Oxide in ZnO-CdS-Ag Ternary Nanocomposite towards Photocatalytic Inactivation of E. Coli under UV and Visible Light. *Chem. Eng. J.* **2017**, *307*, 966−980.
(55) Manchala, S.; Gandamalla, A.; Vempuluru, N. R.; Venkatakrishnan, S. M.; Shanker, V. High Potential and Robust Ternary $LaFeO_3$/CdS/Carbon Quantum Dots Nanocomposite for Photocatalytic H_2 Evolution under Sunlight Illumination. *J. Colloid Interface Sci.* **2021**, *583*, 255−266.
(56) Ahmad, I.; Danish, M.; Khan, A.; Muneer, M. One-Pot Hydrothermal Synthesis of a Double Z-Scheme g-C_3N_4/AgI/β-$AgVO_3$ Ternary Nanocomposite for Efficient Degradation of Organic Pollutants and DPC−Cr (VI) Complex under Visible-Light Irradiation. *Photochem. Photobiol. Sci.* **2022**, *21*, 1371−1386.
(57) Sharma, S.; Qadir, I.; Atri, A. K.; Singh, S.; Manhas, U.; Singh, D. Solvent-Free Combustion-Assisted Synthesis of $LaFe_{0.5}Cr_{0.5}O_3$ Nanostructures for Excellent Photocatalytic Performance toward Water Decontamination: The Effect of Fuel on Structural, Magnetic, and Photocatalytic Properties. *ACS Omega* **2023**, *8*, 555−570.
(58) Danish, M.; Saud Athar, M.; Ahmad, I.; Warshagha, M. Z. A.; Rasool, Z.; Muneer, M. Highly Efficient and Stable Fe_2O_3/g-C_3N_4/GO Nanocomposite with Z-Scheme Electron Transfer Pathway: Role of Photocatalytic Activity and Adsorption Isotherm of Organic Pollutants in Wastewater. *Appl. Surf. Sci.* **2022**, *604*, No. 154604.
(59) Tian, J.; Zhu, Z.; Liu, B. Novel Bi_2MoO_6/Bi_2WO_6/MWCNTs Photocatalyst with Enhanced Photocatalytic Activity towards Degradation of RB-19 under Visible Light Irradiation. *Colloids Surf., A* **2019**, *581*, No. 123798.
(60) Xu, X.; Lin, H.; Xiao, P.; Zhu, J.; Bi, H.; Carabineiro, S. A. C. Construction of Ag-Bridged Z-Scheme $LaFe_{0.5}Co_{0.5}O_3$/Ag_{10}/Graphitic Carbon Nitride Heterojunctions for Photo-Fenton Degradation of Tetracycline Hydrochloride: Interfacial Electron Effect and Reaction Mechanism. *Adv. Mater. Interfaces* **2022**, *9*, No. 2101902.
(61) Alameer, O. O.; Timoumi, A.; El Guesmi, N.; Alamri, S. N.; Belhadj, W.; Althagafi, K.; Ahmed, S. A. Expoloriting of Graphene Oxide for Improving Physical Properties of TiO_2(NPs): Toward Photovoltaic Devices and Wastewater Remediation Approaches. *Eur. Phys. J. Plus* **2022**, *137*, No. 1160.
(62) Wang, H.; Zhang, J.; Yuan, X.; Jiang, L.; Xia, Q. Photocatalytic Removal of Antibiotics from Natural Water Matrices and Swine Wastewater via Cu (I) Coordinately Polymeric Carbon Nitride Framework. *Chem. Eng. J.* **2019**, *392*, No. 123638.
(63) Wang, H.; Wu, Y.; Feng, M.; Tu, W.; Xiao, T.; Xiong, T.; Ang, H.; Yuan, X.; Chew, J. W. Visible-Light-Driven Removal of Tetracycline Antibiotics and Reclamation of Hydrogen Energy from Natural Water Matrices and Wastewater by Polymeric Carbon Nitride Foam. *Water Res.* **2018**, *144*, 215−225.
(64) Jiang, J.; Gao, J.; Li, T.; Chen, Y.; Wu, Q.; Xie, T.; Lin, Y.; Dong, S. Visible-Light-Driven Photo-Fenton Reaction with α-Fe_2O_3/BiOI at near Neutral PH: Boosted Photogenerated Charge Separation, Optimum Operating Parameters and Mechanism Insight. *J. Colloid Interface Sci.* **2019**, *554*, 531−543.
(65) Ibrahim, A. A.; Salama, R. S.; El-Hakam, S. A.; Khder, A. S.; Ahmed, A. I. Synthesis of 12-Tungestophosphoric Acid Supported on Zr/MCM-41 Composite with Excellent Heterogeneous Catalyst and Promising Adsorbent of Methylene Blue. *Colloids Surf., A* **2021**, *631*, No. 127753.
(66) Zhang, J.; Ma, Z.; et al. AgI/β-Ag2MoO4 Heterojunctions with Enhanced Visible-Light-Driven Catalytic Activity. *J. Taiwan Inst. Chem. Eng.* **2017**, *81*, 225−231.
(67) Liu, H.; Hu, C.; Zhai, H.; Yang, J.; Liu, X.; Jia, H. Fabrication of In_2O_3/ZnO@Ag Nanowire Ternary Composites with Enhanced Visible Light Photocatalytic Activity. *RSC Adv.* **2017**, *7*, 37220−37229.
(68) Lv, H.; Duan, Y.; Zhou, X.; Liu, G.; Wang, X.; Wang, Y.; Yuan, M.; Meng, Q.; Wang, C. Visible-Light-Driven Ag/AgCl@In_2O_3: A Ternary Photocatalyst for the Degradation of Tetracycline Antibiotics. *Catal. Sci. Technol.* **2020**, *10*, 8230−8239.
(69) Jamoussi, B.; Chakroun, R.; Timoumi, A.; Essalah, K. Synthesis and Characterization of New Imidazole Phthalocyanine for Photodegradation of Micro-Organic Pollutants from Sea Water. *Catalysts* **2020**, *10*, 906.
(70) Jiang, W.; Li, Z.; Liu, C.; Wang, D.; Yan, G.; Liu, B.; Che, G. Enhanced Visible-Light-Induced Photocatalytic Degradation of Tetracycline Using BiOI/MIL-125(Ti) Composite Photocatalyst. *J. Alloys Compd.* **2021**, *854*, No. 157166.
(71) Gogoi, D.; Makkar, P.; Ghosh, N. N. Solar Light-Irradiated Photocatalytic Degradation of Model Dyes and Industrial Dyes by a Magnetic $CoFe_2O_4$-GC_3N_4 S-Scheme Heterojunction Photocatalyst. *ACS Omega* **2021**, *6*, 4831−4841.
(72) Kaid, M. M.; Khder, A. S.; Ahmed, S. A.; Ibrahim, A. A.; Altass, H. M.; Alsantali, R. I.; Jassas, R. S.; Khder, M. A.; Al-Rooqi, M. M.; Moussa, Z.; Ahmed, A. I. High-Efficacy Hierarchical Dy_2O_3/TiO_2 Nanoflower toward Wastewater Reclamation: A Combined Photoelectrochemical and Photocatalytic Strategy. *ACS Omega* **2022**, *7*, 17223−17233.
(73) Zhang, Q.; Bai, J.; Li, G.; Li, C. Synthesis and Enhanced Photocatalytic Activity of AgI-BiOI/CNFs for Tetracycline Hydrochloride Degradation under Visible Light Irradiation. *J. Solid State Chem.* **2019**, *270*, 129−134.
(74) Athar, M. S.; Danish, M.; Muneer, M. Fabrication of Visible Light-Responsive Dual Z-Scheme (α-Fe_2O_3/CdS/g-C_3N_4) Ternary Nanocomposites for Enhanced Photocatalytic Performance and Adsorption Study in Aqueous Suspension. *J. Environ. Chem. Eng.* **2021**, *9*, No. 105754.

https://doi.org/10.1021/acsomega.3c01517
ACS Omega 2023, 8, 22708−22720

(75) Shi, W.; Liu, C.; Li, M.; Lin, X.; Guo, F.; Shi, J. Fabrication of Ternary $Ag_3PO_4/Co_3(PO_4)_2/g\text{-}C_3N_4$ Heterostructure with Following Type II and Z-Scheme Dual Pathways for Enhanced Visible-Light Photocatalytic Activity. *J. Hazard. Mater.* **2020**, *389*, No. 121907.
(76) Zhang, J.; Ma, Z. Ag_3VO_4/AgI Composites for Photocatalytic Degradation of Dyes and Tetracycline Hydrochloride under Visible Light. *Mater. Lett.* **2018**, *216*, 216−219.
(77) Danish, M.; Muneer, M. Facile Synthesis of Highly Efficient Co@ZnSQDs/$g\text{-}C_3N_4$/MWCNT Nanocomposites and Their Photocatalytic Potential for the Degradation of RhB Dye: Efficiency, Degradation Kinetics, and Mechanism Pathway. *Ceram. Int.* **2021**, *47*, 13043−13056.
(78) Chava, R. K.; Son, N.; Kim, Y. S.; Kang, M. Controlled Growth and Bandstructure Properties of One Dimensional Cadmium Sulfide Nanorods for Visible Photocatalytic Hydrogen Evolution Reaction. *Nanomaterials* **2020**, *10*, 619.

https://doi.org/10.1021/acsomega.3c01517
ACS Omega 2023, 8, 22708−22720